High-speed polarization sensitive optical coherence tomography scan engine based on Fourier domain mode locked laser

Marco Bonesi,[1] Harald Sattmann,[1] Teresa Torzicky,[1] Stefan Zotter,[1] Bernhard Baumann,[1] Michael Pircher,[1] Erich Götzinger,[1] Christoph Eigenwillig,[2] Wolfgang Wieser,[2] Robert Huber,[2] and Christoph K. Hitzenberger[1,*]

[1] *Center for Medical Physics and Biomedical Engineering, Medical University of Vienna, A-1090 Vienna, Austria*
[2] *Lehrstuhl für BioMolekulare Optik, Fakultät für Physik, Ludwig-Maximilians-Universität München, D-80538 München, Germany*
**christoph.hitzenberger@meduniwien.ac.at*

Abstract: We report on a new swept source polarization sensitive optical coherence tomography scan engine that is based on polarization maintaining (PM) fiber technology. The light source is a Fourier domain mode locked laser with a PM cavity that operates in the 1300 nm wavelength regime. It is equipped with a PM buffer stage that doubles the fundamental sweep frequency of 54.5 kHz. The fiberization allows coupling of the scan engine to different delivery probes. In a first demonstration, we use the system for imaging human skin at an A-scan rate of 109 kHz. The system illuminates the sample with circularly polarized light and measures reflectivity, retardation, optic axis orientation, and Stokes vectors simultaneously. Furthermore, depolarization can be quantified by calculating the degree of polarization uniformity (DOPU). The high scanning speed of the system enables dense sampling in both, the x- and y-direction, which provides the opportunity to use 3D evaluation windows for DOPU calculation. This improves the spatial resolution of DOPU images considerably.

OCIS codes: (170.4500) Optical coherence tomography; (230.5440) Polarization-selective devices; (170.4580) Optical diagnostics for medicine.

References and links

1. D. Huang, E. A. Swanson, C. P. Lin, J. S. Schuman, W. G. Stinson, W. Chang, M. R. Hee, T. Flotte, K. Gregory, C. A. Puliafito, and J. G. Fujimoto, "Optical coherence tomography," Science **254**(5035), 1178–1181 (1991).
2. A. F. Fercher, W. Drexler, C. K. Hitzenberger, and T. Lasser, "Optical coherence tomography—principles and applications," Rep. Prog. Phys. **66**(2), 239–303 (2003).
3. W. Drexler and J. G. Fujimoto, *Optical Coherence Tomography. Technology and Applications* (Springer, Berlin, 2008).
4. W. Drexler and J. G. Fujimoto, "State-of-the-art retinal optical coherence tomography," Prog. Retin. Eye Res. **27**(1), 45–88 (2008).
5. J. Welzel, E. Lankenau, R. Birngruber, and R. Engelhardt, "Optical coherence tomography of the human skin," J. Am. Acad. Dermatol. **37**(6), 958–963 (1997).
6. T. Gambichler, G. Moussa, M. Sand, D. Sand, P. Altmeyer, and K. Hoffmann, "Applications of optical coherence tomography in dermatology," J. Dermatol. Sci. **40**(2), 85–94 (2005).
7. M. Mogensen, L. Thrane, T. M. Jørgensen, P. E. Andersen, and G. B. E. Jemec, "OCT imaging of skin cancer and other dermatological diseases," J Biophotonics **2**(6-7), 442–451 (2009).
8. J. Welzel, E. Lankenau, G. Hüttmann, and R. Birngruber, "OCT in dermatology," in *Optical Coherence Tomography: Technology and Applications*, W. Drexler, and J. G. Fujimoto, eds. (Springer, Berlin, 2008), pp. 1103–1122.
9. A. Alex, B. Povazay, B. Hofer, S. Popov, C. Glittenberg, S. Binder, and W. Drexler, "Multispectral in vivo three-dimensional optical coherence tomography of human skin," J. Biomed. Opt. **15**(2), 026025 (2010).
10. G. J. Tearney, M. E. Brezinski, B. E. Bouma, S. A. Boppart, C. Pitris, J. F. Southern, and J. G. Fujimoto, "In vivo endoscopic optical biopsy with optical coherence tomography," Science **276**(5321), 2037–2039 (1997).
11. X. Qi, M. V. Sivak, Jr., and A. M. Rollins, "Optical coherence tomography for gastrointestinal endoscopy," in *Optical Coherence Tomography. Technology and Applications*, W. Drexler, and J. G. Fujimoto, eds. (Springer, Berlin, 2008), pp. 1047–1081.

#176564 - $15.00 USD Received 20 Sep 2012; revised 23 Oct 2012; accepted 23 Oct 2012; pub. 25 Oct 2012

12. G. J. Tearney, S. A. Boppart, B. E. Bouma, M. E. Brezinski, N. J. Weissman, J. F. Southern, and J. G. Fujimoto, "Scanning single-mode fiber optic catheter-endoscope for optical coherence tomography," Opt. Lett. **21**(7), 543–545 (1996).
13. G. J. Tearney, I. K. Jang, and B. E. Bouma, "Imaging coronary atherosclerosis and vulnerable plaques with optical coherence tomography," in *Optical Coherence Tomography. Technology and Applications*, W. Drexler, and J. G. Fujimoto, eds. (Springer, Berlin, 2008), pp. 1083–1101.
14. X. D. Li, S. A. Boppart, J. Van Dam, H. Mashimo, M. Mutinga, W. Drexler, M. Klein, C. Pitris, M. L. Krinsky, M. E. Brezinski, and J. G. Fujimoto, "Optical coherence tomography: advanced technology for the endoscopic imaging of Barrett's esophagus," Endoscopy **32**(12), 921–930 (2000).
15. H. Yabushita, B. E. Bouma, S. L. Houser, H. T. Aretz, I. K. Jang, K. H. Schlendorf, C. R. Kauffman, M. Shishkov, D. H. Kang, E. F. Halpern, and G. J. Tearney, "Characterization of human atherosclerosis by optical coherence tomography," Circulation **106**(13), 1640–1645 (2002).
16. M. R. Hee, D. Huang, E. A. Swanson, and J. G. Fujimoto, "Polarization-sensitive low-coherence reflectometer for birefringence characterization and ranging," J. Opt. Soc. Am. B **9**(6), 903–908 (1992).
17. J. F. de Boer, T. E. Milner, M. J. C. van Gemert, and J. S. Nelson, "Two-dimensional birefringence imaging in biological tissue by polarization-sensitive optical coherence tomography," Opt. Lett. **22**(12), 934–936 (1997).
18. C. K. Hitzenberger, E. Goetzinger, M. Sticker, M. Pircher, and A. F. Fercher, "Measurement and imaging of birefringence and optic axis orientation by phase resolved polarization sensitive optical coherence tomography," Opt. Express **9**(13), 780–790 (2001).
19. B. H. Park, M. C. Pierce, B. Cense, and J. F. de Boer, "Jones matrix analysis for a polarization-sensitive optical coherence tomography system using fiber-optic components," Opt. Lett. **29**(21), 2512–2514 (2004).
20. M. Todorović, S. L. Jiao, L. V. Wang, and G. Stoica, "Determination of local polarization properties of biological samples in the presence of diattenuation by use of Mueller optical coherence tomography," Opt. Lett. **29**(20), 2402–2404 (2004).
21. N. J. Kemp, H. N. Zaatari, J. Park, H. G. Rylander III, and T. E. Milner, "Form-biattenuance in fibrous tissues measured with polarization-sensitive optical coherence tomography (PS-OCT)," Opt. Express **13**(12), 4611–4628 (2005).
22. J. F. de Boer, T. E. Milner, and J. S. Nelson, "Determination of the depth-resolved Stokes parameters of light backscattered from turbid media by use of polarization-sensitive optical coherence tomography," Opt. Lett. **24**(5), 300–302 (1999).
23. J. F. de Boer and T. E. Milner, "Review of polarization sensitive optical coherence tomography and Stokes vector determination," J. Biomed. Opt. **7**(3), 359–371 (2002).
24. S. L. Jiao and L. V. Wang, "Jones-matrix imaging of biological tissues with quadruple-channel optical coherence tomography," J. Biomed. Opt. **7**(3), 350–358 (2002).
25. S. Makita, M. Yamanari, and Y. Yasuno, "Generalized Jones matrix optical coherence tomography: performance and local birefringence imaging," Opt. Express **18**(2), 854–876 (2010).
26. G. Yao and L. V. Wang, "Two-dimensional depth-resolved Mueller matrix characterization of biological tissue by optical coherence tomography," Opt. Lett. **24**(8), 537–539 (1999).
27. S. L. Jiao, M. Todorović, G. Stoica, and L. V. Wang, "Fiber-based polarization-sensitive Mueller matrix optical coherence tomography with continuous source polarization modulation," Appl. Opt. **44**(26), 5463–5467 (2005).
28. E. Götzinger, M. Pircher, W. Geitzenauer, C. Ahlers, B. Baumann, S. Michels, U. Schmidt-Erfurth, and C. K. Hitzenberger, "Retinal pigment epithelium segmentation by polarization sensitive optical coherence tomography," Opt. Express **16**(21), 16410–16422 (2008).
29. E. Götzinger, M. Pircher, B. Baumann, T. Schmoll, H. Sattmann, R. A. Leitgeb, and C. K. Hitzenberger, "Speckle noise reduction in high speed polarization sensitive spectral domain optical coherence tomography," Opt. Express **19**(15), 14568–14585 (2011).
30. M. Pircher, C. K. Hitzenberger, and U. Schmidt-Erfurth, "Polarization sensitive optical coherence tomography in the human eye," Prog. Retin. Eye Res. **30**(6), 431–451 (2011).
31. J. F. De Boer, S. M. Srinivas, A. Malekafzali, Z. P. Chen, and J. S. Nelson, "Imaging thermally damaged tissue by polarization sensitive optical coherence tomography," Opt. Express **3**(6), 212–218 (1998).
32. C. E. Saxer, J. F. de Boer, B. H. Park, Y. H. Zhao, Z. P. Chen, and J. S. Nelson, "High-speed fiber based polarization-sensitive optical coherence tomography of in vivo human skin," Opt. Lett. **25**(18), 1355–1357 (2000).
33. B. H. Park, C. Saxer, S. M. Srinivas, J. S. Nelson, and J. F. de Boer, "In vivo burn depth determination by high-speed fiber-based polarization sensitive optical coherence tomography," J. Biomed. Opt. **6**(4), 474–479 (2001).
34. M. C. Pierce, R. L. Sheridan, B. Hyle Park, B. Cense, and J. F. de Boer, "Collagen denaturation can be quantified in burned human skin using polarization-sensitive optical coherence tomography," Burns **30**(6), 511–517 (2004).
35. M. Pircher, E. Goetzinger, R. Leitgeb, and C. K. Hitzenberger, "Three dimensional polarization sensitive OCT of human skin in vivo," Opt. Express **12**(14), 3236–3244 (2004).
36. K. H. Kim, J. A. Burns, J. J. Bernstein, G. N. Maguluri, B. H. Park, and J. F. de Boer, "In vivo 3D human vocal fold imaging with polarization sensitive optical coherence tomography and a MEMS scanning catheter," Opt. Express **18**(14), 14644–14653 (2010).
37. S. K. Nadkarni, M. C. Pierce, B. H. Park, J. F. de Boer, P. Whittaker, B. E. Bouma, J. E. Bressner, E. Halpern, S. L. Houser, and G. J. Tearney, "Measurement of collagen and smooth muscle cell content in atherosclerotic plaques using polarization-sensitive optical coherence tomography," J. Am. Coll. Cardiol. **49**(13), 1474–1481 (2007).

38. M. C. Pierce, M. Shishkov, B. H. Park, N. A. Nassif, B. E. Bouma, G. J. Tearney, and J. F. de Boer, “Effects of sample arm motion in endoscopic polarization-sensitive optical coherence tomography,” Opt. Express **13**(15), 5739–5749 (2005).
39. D. P. Davé, T. Akkin, and T. E. Milner, “Polarization-maintaining fiber-based optical low-coherence reflectometer for characterization and ranging of birefringence,” Opt. Lett. **28**(19), 1775–1777 (2003).
40. M. K. Al-Qaisi and T. Akkin, “Polarization-sensitive optical coherence tomography based on polarization-maintaining fibers and frequency multiplexing,” Opt. Express **16**(17), 13032–13041 (2008).
41. A. F. Fercher, C. K. Hitzenberger, G. Kamp, and S. Y. Elzaiat, “Measurement of intraocular distances by backscattering spectral interferometry,” Opt. Commun. **117**(1-2), 43–48 (1995).
42. Y. Yasuno, S. Makita, Y. Sutoh, M. Itoh, and T. Yatagai, “Birefringence imaging of human skin by polarization-sensitive spectral interferometric optical coherence tomography,” Opt. Lett. **27**(20), 1803–1805 (2002).
43. R. Leitgeb, C. K. Hitzenberger, and A. F. Fercher, “Performance of fourier domain vs. time domain optical coherence tomography,” Opt. Express **11**(8), 889–894 (2003).
44. J. F. de Boer, B. Cense, B. H. Park, M. C. Pierce, G. J. Tearney, and B. E. Bouma, “Improved signal-to-noise ratio in spectral-domain compared with time-domain optical coherence tomography,” Opt. Lett. **28**(21), 2067–2069 (2003).
45. M. A. Choma, M. V. Sarunic, C. H. Yang, and J. A. Izatt, “Sensitivity advantage of swept source and Fourier domain optical coherence tomography,” Opt. Express **11**(18), 2183–2189 (2003).
46. K. H. Kim, B. H. Park, G. N. Maguluri, T. W. Lee, F. J. Rogomentich, M. G. Bancu, B. E. Bouma, J. F. de Boer, and J. J. Bernstein, “Two-axis magnetically-driven MEMS scanning catheter for endoscopic high-speed optical coherence tomography,” Opt. Express **15**(26), 18130–18140 (2007).
47. W. Y. Oh, S. H. Yun, B. J. Vakoc, M. Shishkov, A. E. Desjardins, B. H. Park, J. F. de Boer, G. J. Tearney, and B. E. Bouma, “High-speed polarization sensitive optical frequency domain imaging with frequency multiplexing,” Opt. Express **16**(2), 1096–1103 (2008).
48. R. Huber, M. Wojtkowski, and J. G. Fujimoto, “Fourier Domain Mode Locking (FDML): A new laser operating regime and applications for optical coherence tomography,” Opt. Express **14**(8), 3225–3237 (2006).
49. W. Wieser, B. R. Biedermann, T. Klein, C. M. Eigenwillig, and R. Huber, “Multi-megahertz OCT: High quality 3D imaging at 20 million A-scans and 4.5 GVoxels per second,” Opt. Express **18**(14), 14685–14704 (2010).
50. E. Götzinger, B. Baumann, M. Pircher, and C. K. Hitzenberger, “Polarization maintaining fiber based ultra-high resolution spectral domain polarization sensitive optical coherence tomography,” Opt. Express **17**(25), 22704–22717 (2009).
51. H. Wang, M. K. Al-Qaisi, and T. Akkin, “Polarization-maintaining fiber based polarization-sensitive optical coherence tomography in spectral domain,” Opt. Lett. **35**(2), 154–156 (2010).
52. T. Torzicky, M. Pircher, S. Zotter, M. Bonesi, E. Götzinger, and C. K. Hitzenberger, “Automated measurement of choroidal thickness in the human eye by polarization sensitive optical coherence tomography,” Opt. Express **20**(7), 7564–7574 (2012).
53. M. K. Al-Qaisi and T. Akkin, “Swept-source polarization-sensitive optical coherence tomography based on polarization-maintaining fiber,” Opt. Express **18**(4), 3392–3403 (2010).
54. R. Huber, D. C. Adler, and J. G. Fujimoto, “Buffered Fourier domain mode locking: Unidirectional swept laser sources for optical coherence tomography imaging at 370,000 lines/s,” Opt. Lett. **31**(20), 2975–2977 (2006).
55. R. Huber, D. C. Adler, V. J. Srinivasan, and J. G. Fujimoto, “Fourier domain mode locking at 1050 nm for ultra-high-speed optical coherence tomography of the human retina at 236,000 axial scans per second,” Opt. Lett. **32**(14), 2049–2051 (2007).
56. G. Palte, W. Wieser, B. R. Biedermann, C. M. Eigenwillig, and R. Huber, “Fourier Domain Mode Locked (FDML) Lasers for Polarization Sensitive OCT,” Proc. SPIE **7372**, 73720M, 73720M-6 (2009).
57. J. Zhang, J. Jing, P. Wang, and Z. Chen, “Polarization-maintaining buffered Fourier domain mode-locked swept source for optical coherence tomography,” Opt. Lett. **36**(24), 4788–4790 (2011).
58. W. Wieser, G. Palte, C. M. Eigenwillig, B. R. Biedermann, T. Pfeiffer, and R. Huber, “Chromatic polarization effects of swept waveforms in FDML lasers and fiber spools,” Opt. Express **20**(9), 9819–9832 (2012).
59. E. Götzinger, M. Pircher, and C. K. Hitzenberger, “High speed spectral domain polarization sensitive optical coherence tomography of the human retina,” Opt. Express **13**(25), 10217–10229 (2005).
60. A. M. Rollins, R. Ung-Arunyawee, A. Chak, R. C. K. Wong, K. Kobayashi, M. V. Sivak, Jr., and J. A. Izatt, “Real-time in vivo imaging of human gastrointestinal ultrastructure by use of endoscopic optical coherence tomography with a novel efficient interferometer design,” Opt. Lett. **24**(19), 1358–1360 (1999).
61. P. R. Herz, Y. Chen, A. D. Aguirre, K. Schneider, P. Hsiung, J. G. Fujimoto, K. Madden, J. Schmitt, J. Goodnow, and C. Petersen, “Micromotor endoscope catheter for in vivo, ultrahigh-resolution optical coherence tomography,” Opt. Lett. **29**(19), 2261–2263 (2004).

---

1. Introduction

Optical coherence tomography (OCT) has been introduced two decades ago [1] as a non-invasive modality for imaging transparent and translucent tissues with resolution of a few µm [2,3]. The first (and still dominating) application field of OCT was, because of the high transparency of ocular media, ophthalmology, where OCT revolutionized retinal diagnostics [4]. OCT is also very useful to image scattering tissues down to a depth of ~1–2 mm. An organ particularly suited for OCT imaging is, because of its direct accessibility to the optical

#176564 - $15.00 USD Received 20 Sep 2012; revised 23 Oct 2012; accepted 23 Oct 2012; pub. 25 Oct 2012

radiation, the skin. Therefore, it is not surprising that dermatologic applications of OCT were introduced quite early [5]. Meanwhile, several dermatologic applications of OCT were reported (see, e.g., [6–8]) and the effect of wavelength for different purposes of skin imaging was analyzed [9]. Other tissues of interest for OCT imaging are those accessible by endoscopic probes, like the mucosa of the gastro-intestinal tract [10,11] and vessels [12,13]. Several applications of endoscopic OCT have been reported, ranging from Barrett's esophagus [14] to differentiation of various types of plaques in vessel walls [15].

While commercial OCT scanners for dermatologic and endoscopic applications are now available and have been used for imaging of various lesions, they still have a drawback: they record images only on an intensity basis and therefore do not exploit the full information available in the backscattered light. Polarization sensitive (PS) OCT overcomes this limitation [16,17]. By illuminating the sample with one or more well defined polarization states, and by performing a polarization sensitive detection that splits the interfering beams in the detection arm into two orthogonally polarized components that are measured in parallel, several quantities like retardation [16,17], optic axis orientation [18], diattenuation [19–21], Stokes vectors [22,23], and Jones [19,24,25] and Müller matrices [26,27] can be measured. In addition, a quantity related to the degree of polarization (which is not directly accessible by OCT), the (spatially or temporally averaged) degree of polarization uniformity (DOPU) [28,29] can be obtained by PS-OCT.

Although the majority of PS-OCT work reported to date is related to ophthalmology [30], dermatology was one of its first applications [31,32]. The change in skin birefringence caused by thermal denaturation of collagen suggested PS-OCT application for burn depth imaging [33,34]. These and other [35] early applications of PS-OCT to skin imaging were based on bulk optic time domain OCT. Endoscopic applications of OCT require fiber optics. This complicates the setup because usual single mode fibers don't preserve the polarization state of the backscattered beam. However, endoscopic PS-OCT applications seem attractive in applications like laryngoscopy, where it has been shown that the regular birefringence pattern of the vocal folds is destroyed in cancerous lesions [36], or in cardiovascular imaging where PS-OCT was suggested to be used for evaluating the stability of atherosclerotic plaques [37]. The introduction of systems using multiple input polarization states [33] solved the problems mentioned above and enabled endoscopic PS-OCT [38], however, at the cost of higher system complexity. First applications of polarization maintaining (PM) fibers were implemented in time domain technology and required either splicing of two PM fibers with exactly equal length (which is difficult to achieve), where the slow axis of the first fiber was coupled to the fast axis of the second fiber, and vice versa [39], or the implementation of an additional pair of compensating birefringent wedges that had to be carefully adjusted to compensate the optical path length difference introduced by the PM fibers [40].

While the early applications of PS-OCT were based, as all the early OCT work, on time domain OCT, Fourier domain methods [41] were demonstrated for PS-OCT skin imaging as early as 2002 [42], one year before the Fourier domain sensitivity advantage was discovered [43–45]. After this discovery, dermatologic and endoscopic PS-OCT imaging also switched to Fourier domain methods, either to spectrometer based (SD) techniques [46] or to swept source (SS) technology [47]. While both, SD and SS OCT show the same sensitivity advantage, SS-OCT has recently attracted more interest in the wavelength range around 1300 nm (which is usually applied for imaging of scattering tissues) because of the technology boost of swept sources. Especially the introduction of the Fourier domain mode locked (FDML) laser [48] has enabled imaging speeds of > 100 kA-lines/s, with recent records in the MHz range [49].

We recently developed various PS-OCT systems for ophthalmic applications that use only a single input polarization state to measure reflectivity, retardation, optic axis orientation, Stokes vectors and DOPU simultaneously. The latest versions of these instruments are based on SD technique using a PM fiber based Michelson interferometer [50,51] and on SS technique using a bulk optics Mach–Zehnder interferometer in combination with a PM fiber optic polarization sensitive detection arm [52]. The more complicated Mach–Zehnder interferometer was chosen in the latter case since it directly enables dual balanced detection which is required to reduce noise in SS OCT. (A related alternative approach employing a PM fiber based Michelson interferometer and additional bulk optics components was recently reported [53].)

It is the purpose of this work to combine the principles of these two systems to develop a new, versatile fiber optic high-speed PS-OCT scan engine based on a passively polarization stabilized FDML laser that operates at a speed beyond 100 kA-lines/s. The system is based on PM fiber technology and shall, in the final stage, enable dermatologic and endoscopic imaging via coupling to various flexible probes. In a first stage, we describe the scan engine, report on its parameters, and demonstrate its application for imaging various areas of human skin in vivo. Furthermore, as an example of the increased benefit of high-speed imaging, we demonstrate, for the first time, the use of a new 3D windowing technique that improves the spatial resolution of DOPU images considerably.

2. Methods

We have developed a PM fiber based PS-OCT scan engine that allows fast in-vivo and noninvasive biomedical imaging of biological samples and demonstrate its use for skin imaging. Our system is based on methods previously reported for spectrometer based (SD) instruments [50] and was modified to accommodate the special requirements of swept source technique.

2.1. FDML swept laser source

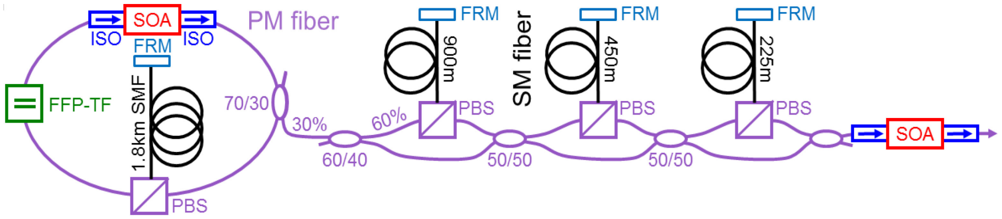

Fig. 1. Layout of FDML laser and buffer stage (only the first buffer stage was used in the experiments described here, the second and third buffer stages were disconnected). FFP-TF, fiber Fabry-Perot tunable filter; ISO, isolator; SOA, semiconductor optical amplifier; FRM, Faraday rotation mirror; PBS, polarizing beam splitter; SM, single mode; PM, polarization maintaining.

The built PS-OCT system makes use of a custom-developed high-speed broadband Fourier-Domain Mode Locked (FDML) swept laser source operating in the region of 1300 nm wavelength. The sweep frequency of the FDML laser is doubled by using an external buffer stage. Principles, technical and functional details of buffered FDML swept laser sources have been previously reported [48,54–58]. Figure 1 shows the layout of the FDML laser and buffer stage (please note that only the first buffer stage was used for the experiments described here; the second and third buffer stages, which can be used to increase the scanning speed by factors 4 and 8 were disconnected). The laser and the buffer stage were designed to maintain the polarization state of the light. For this purpose, PM panda fibers and PM fiber components were used throughout most parts of the laser. To avoid excessive costs of long PM fibers, the delay fibers are standard single mode (SM) fibers. However, the application of a Faraday rotation mirror (FRM) and a double pass lead to an efficient cancellation of all polarization rotation effects in the delay fibers. Therefore, the combination of the three elements: polarizing beam splitter (PBS), standard SM fiber and FRM is polarization maintaining [58]. This approach has the main advantages of a reliable preservation of the polarization state of the light inside the FDML laser and a simplification of the fiber-based connection between the FDML laser and the buffer stage, by avoiding the needs of inserting additional polarization control elements, e.g. polarization paddles, between the two devices.

The physical cavity length of the laser used here yields a fundamental optical roundtrip frequency of 54.5 kHz; this basic sweep frequency was doubled to 109 kHz by the buffer stage. The duty cycle of our system, including the buffer stage, is ~80%. The source central wavelength, λ_0, and spectral bandwidth, $\Delta\lambda$, are user-tunable and, for optimal OCT imaging performances, these parameters—with other FDML laser driving signals—need to be fine-adjusted according to the specific sweep frequency imposed by the laser cavity length. For the experiments reported here, λ_0 was set to 1315 nm, providing a sweep range of $\Delta\lambda = 120$ nm (after the buffer stage), and an output power of 23.9 mW.

2.2. PS-OCT system description

The fiber-based PS-OCT system was built using PM panda fibers and PM panda fiber-based optical components. With reference to Fig. 2, the polarized light emitted by the FDML laser source is launched into the input port (c1) of the circulator (OLCIR-P-3-131-300-90-FP, Opto-Link, Hong Kong). The circulator has special polarization properties: light coupled from port c1 to c2 is linearly polarized, while light coupled from port c2 to c3 maintains its polarization state. Therefore the light exiting from the second port (c2) is linearly polarized along the slow axis of the PM fiber. Port c2 is coupled to the input port (t1) of the 50/50 optical coupler (OLCPL-T-P-22-131-50-90-FP-B, Opto-Link, Hong Kong). Sample and reference arms contain 30 m of PM fiber, each, to shift ghost images (caused by cross-coupling into the other polarization channel) out of the visible image range.

The reference light exiting the PM fiber of the 50:50 coupler is linearly polarized along the slow axis of the fiber. It traverses a quarter wave plate (QWP) oriented at 22.5° to the slow axis. After reflection at the reference mirror and double passing the QWP, the light is in a

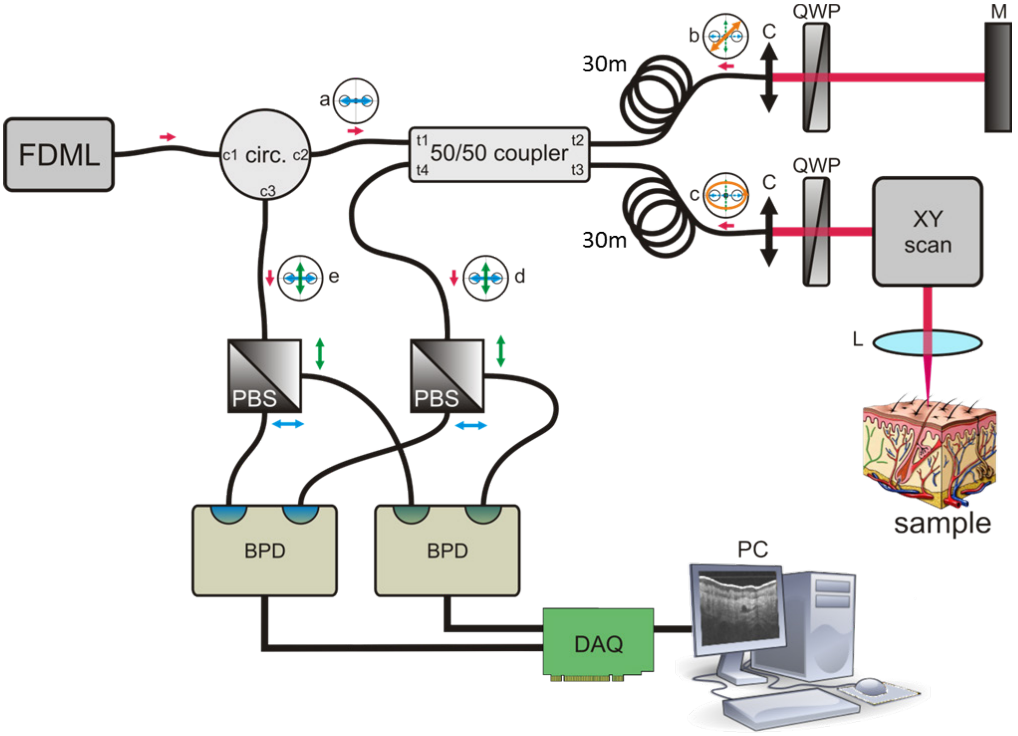

Fig. 2. Sketch of PM fiber-based PS-OCT setup. FDML, Fourier-domain mode-locked swept laser source and buffer stage; circ. –circulator; C, collimator; 30 m, 30 m long PM fibers; QWP, quarter wave plate; M, mirror; XY scan, galvo scanner; L, sample arm lens; PBS, polarizing beam splitter; BPD, balanced photodetector; DAQ, data acquisition card; PC, personal computer; a-e, representation of theoretical polarization state of the probing radiation.

linear polarization state oriented at 45°, providing equal reference power in both, the fast and the slow axes of the fiber, and thus in the two orthogonal polarization states into which the light is split by the polarizing fiber beam splitter PBS.

The sample light exiting the sample arm fiber is also polarized along the slow axis of the fiber. It traverses a QWP oriented at 45°, providing circularly polarized light to the sample. The beam is raster scanned over the sample using an x-y galvo scanner and a focusing lens of 50 mm focal length. After backscattering by the sample and traversing the QWP a second time, the sample light is in an elliptical polarization state. This state has to be measured to retrieve the sample's polarizing properties. On back-coupling into the PM fiber of the sample arm, the beam is decomposed into two orthogonal states. While the amplitudes of the electric field components of the light travelling along the two polarization axes of the PM fiber is maintained and can be retrieved directly, the phase difference is altered by the different propagation speeds of the two components and has to be retrieved by an additional post processing step [50].

Sample and reference beams interfere in the 50:50 PM fiber coupler, and the interfering light beams exiting ports t1 and t4 of the coupler are guided towards two polarizing fiber beam splitters PBS (OLCS-12-131-90-S1-75-FP, Opto-Link, Hong Kong): one component directly via port t4, the other via port t1 and the circulator that maintains the polarization state, as mentioned above. To avoid phase shifts between the oscillating interference signals travelling along the different parts (which would disturb dual balanced detection), the total lengths of the two fibers guiding the two components are matched. The fibers connecting the circulator, the 50:50 coupler and the two polarizing beam splitters were spliced to avoid cross coupling of polarization states. The output ports of the horizontal polarization state of the two PBS were plugged into a dual balanced photodetector (Thorlabs, PDB130C, 350 MHz) and, similarly, the two output ports of the vertical polarization state of the two PBS were plugged into the other photodetector (same model) to convert the optic signal into an electric equivalent, enabling dual balanced detection. The two electric signals are digitized by a two-channel high speed data acquisition board (Alazartech, ATS9870, 1GS/s, 8 bit). Data acquisition and operation of the galvo scanners are synchronized and controlled by a field programmable gate array (FPGA) board (National Instruments), employing custom software developed under LabView (National Instruments) environment.

With a power of ~5 mW at the sample, we measured a sensitivity of 110 dB near zero delay with a roll-off of ~3 dB over the first mm; for larger distances (1–4 mm), the decay was ~6 dB/mm (cf. Fig. 3). The maximum imaging range (determined by the highest frequency the

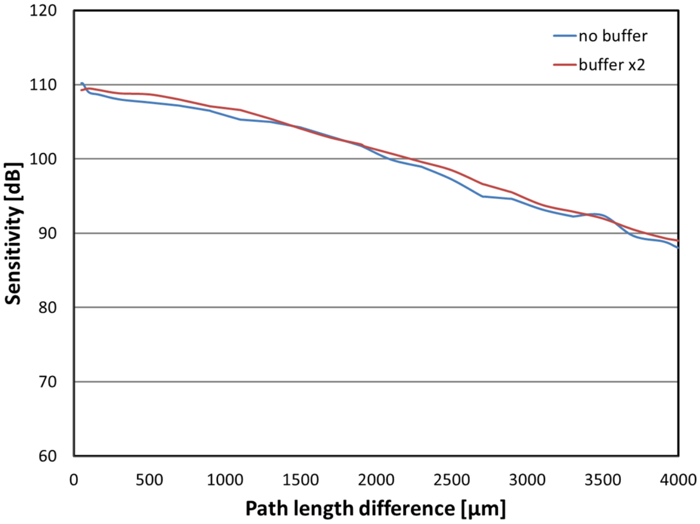

Fig. 3. Sensitivity and roll-off of the PS-OCT system.

#176564 - $15.00 USD Received 20 Sep 2012; revised 23 Oct 2012; accepted 23 Oct 2012; pub. 25 Oct 2012

system can measure) is ~7.5 mm. Because of practical reasons (sensitivity decay, penetration depth), we limited the imaging depth to ~2.5 mm in the experiments shown here. The dynamic range within reflectivity images was ~40–45 dB. The measured axial resolution (FWHM width of point spread function (PSF)) was 6.5 µm in air. This resolution was measured at an imaging depth of 0.625 mm, approximately the midpoint of useful depth scan range for skin imaging. The resolution slightly degrades for larger and shorter path delays. This increase of PSF width is due to non-perfect system dispersion compensation, originating from both the FDML source and the fiber-based optical setup, and consequently incorrect rescaling of acquired spectral data into equidistant data points in k-space. However, the deviation within the imaging range required for skin imaging is negligible.

2.3. Data acquisition and processing

To perform skin imaging, a volumetric data acquisition scan protocol based on a raster scan pattern was implemented. The protocol includes simultaneous acquisition of data from both polarization channels. For each channel, the acquired volume is composed of a user-selected number of frames (B-scans), each of which consists of a user-selected number of records (A-scans). Typical values are 256 B-scans × 1024 A-scans. The geometrical dimensions (width and height) of the scan area on the sample, expressed in mm, are also user-selectable, to enable flexible adaptation of the desired imaging surface area according to the selected volume size (records × frames).

Fourier domain OCT methods require that the data are sampled equidistant in wavenumber (k) space. Since the Fabry-Perot tunable filter of the swept source is driven with a sinusoidal signal and no k-clocking is implemented, numerical rescaling of the raw signal is performed to compensate for the non-linear sweep. For this purpose, a calibration signal is recorded prior to imaging by placing a mirror in the sample arm. The recorded signal is then used to measure sweep nonlinearities and to correct signals that are recorded in the following imaging session by resampling them to be linear in k-space.

Data pre-processing comprises the following steps: removal of fixed pattern noise (caused by internal reflections), data resampling to be linear in k-space (see above), numerical dispersion compensation, and inverse FFT. Optionally, spectral side lobe suppression by windowing and zero padding can be applied. From the complex data sets provided by the inverse FFT, amplitude and phase information are extracted. These steps are performed for both polarization channels.

In a next step, reflectivity and polarization parameters are calculated. While the amplitude of the signals obtained can be directly used to derive reflectivity and retardation [18,59], the phase difference between the two signals, which is required to calculate axis orientation and Stokes vectors [18,28,59], has to be corrected for an offset introduced by the PM fibers. This is done by a numerical method recently described [50]. (It should be mentioned that this method of phase offset correction provides only short-time stability, i.e., only relative axis orientation and variation within an image can be measured.) As a final parameter, DOPU is calculated from the Stokes vector data (not shown here) by spatial averaging of Stokes vector elements in a floating evaluation window. Details of the algorithm can be found in ref [28]. For the polarization data to be reliable, the signal-to-noise ratio of the signal amplitude has to be above a certain threshold for the corresponding pixel. To avoid display of unreliable data points, all the image points that don't meet that criterion are displayed in gray in the polarization images.

In addition to the previously described averaging within 2D windows located within a single B-scan, we present here, for the first time, results of averaging over 3D windows that extend over adjacent B-scans. The size (width (x), height (y), and depth (z), in pixels) of the 3D window is conveniently chosen to include, on one hand, a significant number of data points available for Stokes vector elements statistics, and, on the other hand, to improve resolution within a B-scan. The trade-off limits between these two opposite aspects of DOPU computation, as previously described for 2D windowing [28], are now improved (cf. section 3). Assuming that a floating evaluation window composed of e.g. 96 voxels represents a meaningful statistical set to compute the value of a pixel of a DOPU tomogram, a 2D window will distribute these elements over a rectangular area, e.g. 12 × 8 pixels (width × depth), within a single B-scan. The resolution of the DOPU image will correspond to the geometrical dimension of the 2D window. A 3D window, e.g. of 6 × 4 × 4 pixels (width × depth × height) will distribute the same number of voxels over a volume composed of smaller areas (6 × 4, width × depth) within each B-scan and distributed over several subsequent B-scans (× 4, height). In this case, the resolution of the DOPU image using 3D windowing will correspond to the 3D window width × depth, while carrying the statistical information of the whole 3D window volume. High A-scan rate in conjunction with fast data acquisition and storage makes it possible to acquire large data volumes with high sample density along the y direction (height) while minimizing distortion effects due to sample motion. This enables meaningful 3D window DOPU computation on the acquired volume with better spatial resolution.

Due to limited processing speed, the instrument has different operation modes. A preview/alignment mode that is used to get a coarse overview of the imaged area and to optimize the alignment of scanning optics with respect to the sample: In this mode, a reduced amount of data (128 A-scans/B-scan) is recorded and displayed online in real time (just the intensity image of a single channel). Once alignment is adjusted, the recording mode is activated and an entire 3D data set is recorded. After recording of the data set, the calculation of the polarization parameters, as described above, is performed offline for the full data set. The calculation time is ~200 seconds for a 3D data set of 1024 × 256 A-scans (which includes reflectivity, retardation, and axis orientation images). DOPU images are calculated optionally, the processing time depending on the evaluation window size.

3. Results

Figure 4 shows PS-OCT skin images recorded across the proximal interphalangeal joint of the middle finger. Figures 4(a), 4(b), 4(c), and 4(d), are single-frame reflectivity, retardation, axis orientation, and DOPU B-scans, respectively. Figures 4(e), 4(f), and 4(g) show averaged B-scans of reflectivity, retardation, and axis orientation (average of 15 frames recorded at the same position, methods of averaging: see ref [29]; as an additional processing step for generating averaged images, residual motion artifacts between the individual frames were corrected by image cross correlation methods). The improvement of image quality and the reduction of speckle noise achieved by averaging are clearly observed. Figure 4(h) shows a photograph of the scan location.

The reflectivity images show several layers of skin: stratum corneum (SC), epidermis, dermis, and structures of low reflectivity, probably vessels or fat. The retardation and axis orientation images show areas of varying retardation and axis orientation within epidermis and dermis. Interestingly, the retardation frequently stays rather constant below the stratum corneum, giving rise to a column-like structure in these images. It seems that the retardation has largely built up within the superficial SC, which is therefore birefringent. The light directly backscattered by the SC is in a random polarization state (i.e., depolarized), which is clearly observed by the random color distribution of pixels within this layer in the retardation and axis orientation images. This can also be observed in the DOPU image (d) which shows very low DOPU values within the SC. A similar effect has been reported in one of our early PS-OCT studies using a time domain PS-OCT setup [35].

Figure 5 shows PS-OCT images of a human nail fold. The images were taken from a 3D data set covering a volume of 6(x) × 3(y) × 2.2(z, optical distance) mm^3. Figures 5(a), 5(b), 5(c), and 5(d) are single-frame B-scans of reflectivity, retardation, axis orientation, and DOPU, respectively. The skin (left-hand sides of the images) shows birefringence with varying amount of retardation and axis orientation. The DOPU image 5(d) clearly shows depolarization (low DOPU values indicated by blue-green colors) in the SC layer, while deeper layers show a rather well-defined polarization state. The nail plate (right-hand side of images) shows a depolarizing superficial layer and strong birefringence (a total of three retardation oscillations) in the retardation image 5(b). The axis orientation image also shows color oscillations which, however, are not caused by a true axis change but by the algorithm

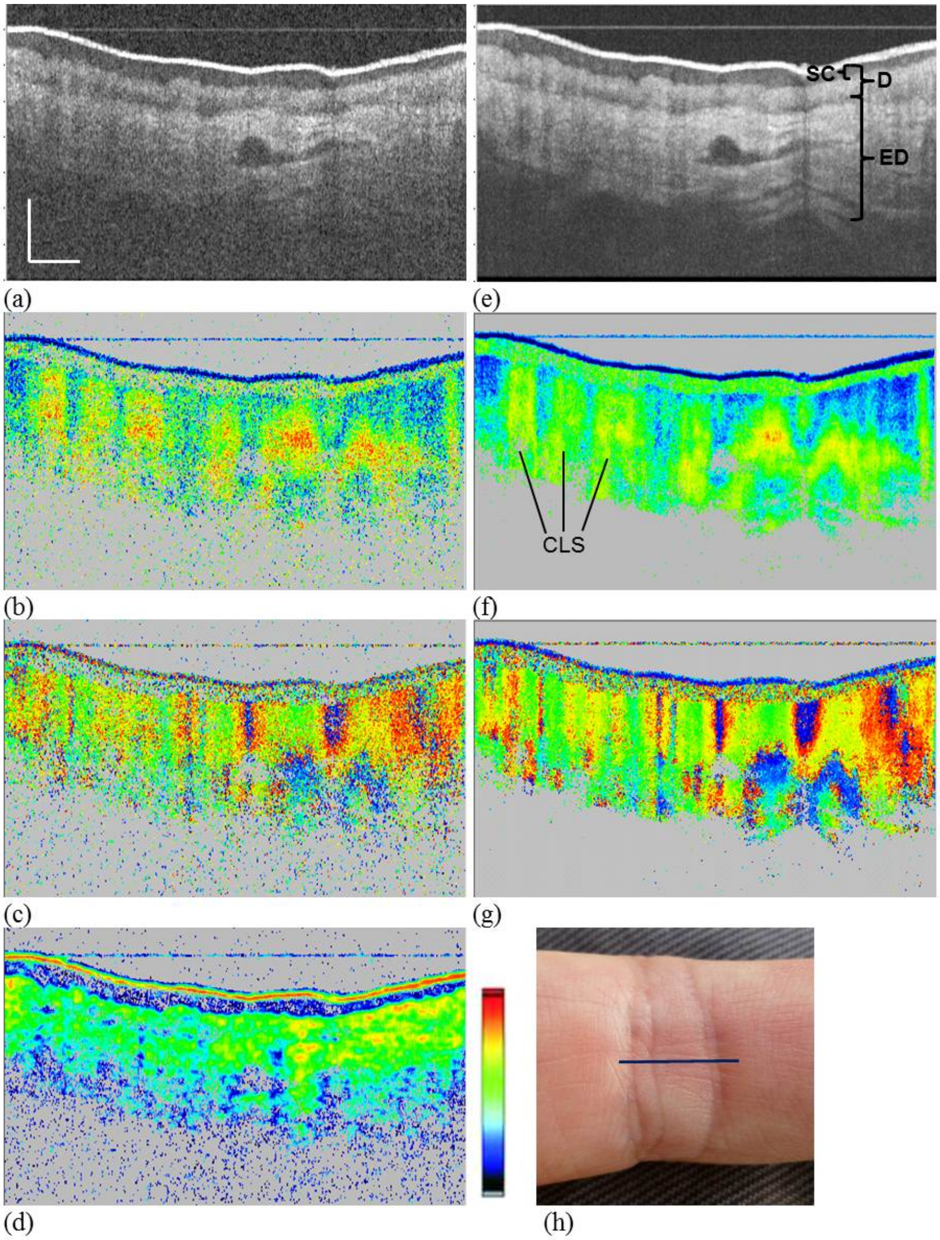

Fig. 4. PS-OCT images of human skin. Proximal interphalangeal joint of middle finger (PIP) region. (a)–(d) single frame images; (e)–(g) average of 15 frames. (a), (e) reflectivity (log scale); (b), (f) retardation (color scale: 0°–90°); (c), (g) axis orientation (color scale, –90° to +90°); (d) DOPU (color scale, 0–1), 2D DOPU window (12(x) × 6(z) pixels or 55 × 38 μm^2); (h) photo of imaged area, line shows approximate B-scan position. Scale bar dimensions: 0.5 mm (x, geometrical distance; z, optical distance). SC, stratum corneum; ED, epidermis; D, dermis; CLS, "column" like structure.

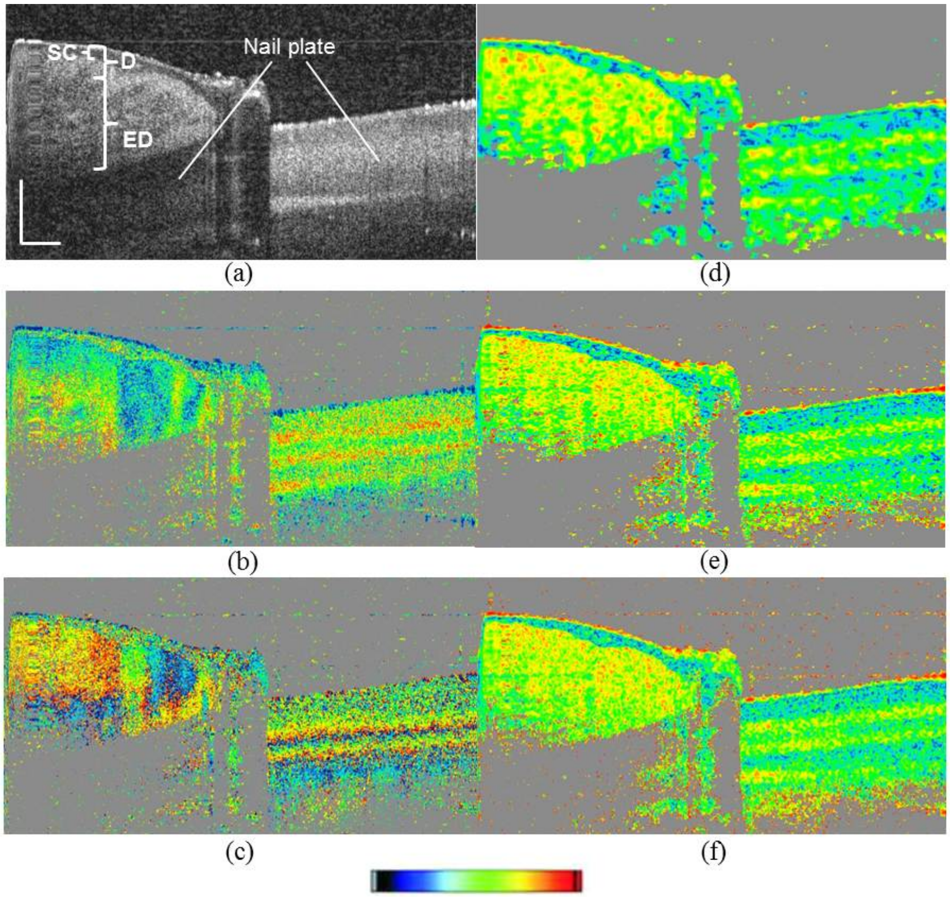

(a) (d)

(b) (e)

(c) (f)

Fig. 5. PS-OCT images of human skin. Nail fold region. (a) reflectivity (log scale); (b) retardation (color scale: 0°–90°); (c) axis orientation (color scale: −90° to +90°); (d)–(f) DOPU (color scale: 0–1). (d) 2D DOPU window (16(x) × 7(z) pixels or 96 × 44 μm^2); (e) 3D DOPU window (8(x) × 4(y) × 3(z) pixels or 48 × 48 × 19 μm^3); (f) 3D DOPU window (5(x) × 5(y) × 3(z) pixels or 30 × 60 × 19 μm^3). Scale bar dimensions: 0.5 mm (x: geometrical distance; z: optical distance). SC, stratum corneum; ED, epidermis; D, dermis.

used to calculate the axis. This algorithm causes a color jump by 90° at positions where the retardation value passes 90° (or multiples of 90°) [18].

While in Fig. 5(d) DOPU was calculated by averaging Stokes vector elements within a 2D evaluation window (size: 7(z) × 16(x) pixels within the B-scan), Figs. 5(e) and 5(f) employ 3D evaluation windows (5(e), 3(z) × 8(x) × 4(y) pixels; 5(f), 3(z) × 5(x) × 5(y) pixels). The use of smaller in-plane areas (3 × 8 or 3 × 5 pixels instead of 7 × 12 pixels) which is enabled by the use of 3D data sets clearly improves the resolution within the DOPU images.

Figure 6 shows PS-OCT images of a human fingertip. The images were taken from a 3D data set covering a volume of 8(x) × 2(y) × 1.9(z, optical distance) mm^3. Figures 6a, 6(b), 6(c), and 6(d) are single frame B-scans of reflectivity, retardation, axis orientation, and DOPU, respectively. The SC is rather thick at this region of skin and strongly depolarizing, as can be seen by the random color values observed in the retardation and axis orientation images, as well as by the low DOPU values (Fig. 6(d)). Similar to Fig. 4, birefringence-induced "columns" of increased retardation can be observed in the tissues below the SC (associated with axis orientations that vary between the different "columns"). Since colors stay essentially constant with depth, most of the retardation is introduced within the SC.

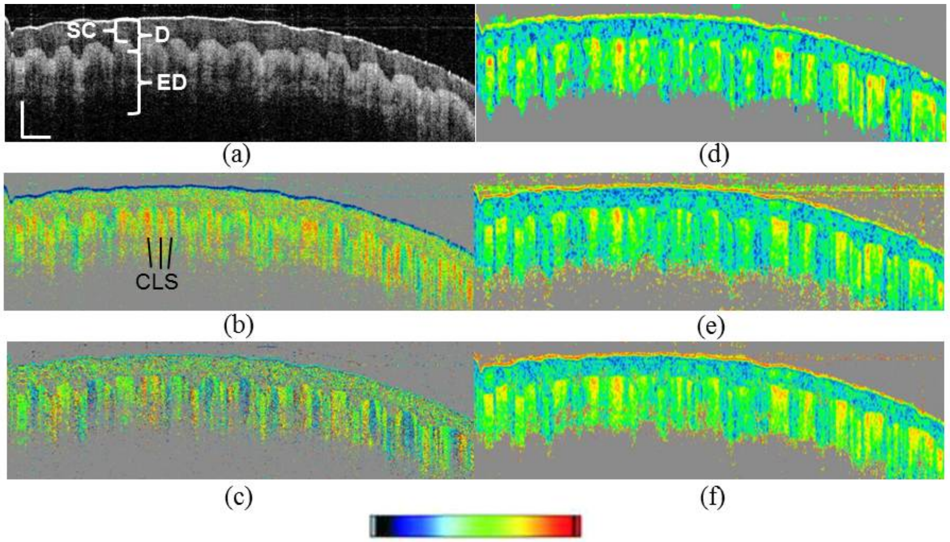

Fig. 6. PS-OCT images of human skin. Fingertip region. (a) reflectivity (log scale); (b) retardation (color scale: 0°–90°); (c) axis orientation (color scale: −90° to +90°); (d)–(f) DOPU (color scale: 0–1). (d) 2D DOPU window (6(x) × 12(z) pixels or 48 × 75 μm^2); (e) 3D DOPU window (4(x) × 4(y) × 6(z) pixels or 32 × 32 × 38 μm^3); (f) 3D DOPU window (2(x) × 6(y) × 6(z) pixels or 16 × 48 × 38 μm^3). Scale bar dimensions: 0.5 mm (x: geometrical distance; z: optical distance). SC, stratum corneum;, ED, epidermis; D, dermis; CLS, "column" like structure.

Contrary to Fig. 4, the retardation "columns" are very narrow in Fig. 6. This disturbs the DOPU algorithm. Since transverse changes of retardation occur on a narrow spatial scale, the polarization state varies within the DOPU evaluation window. Since the DOPU algorithm cannot differentiate between this effect and a randomly varying polarization state (as caused by depolarization), the DOPU image also shows vertical stripes of low DOPU (indicating the transition zones between the different retardation "columns"). The use of 3D DOPU windows (Fig. 6(e), window size: 6(z) × 4(x) × 4(y) pixels; and Fig. 6(f), window size: 6(z) × 2(x) × 6(y) pixels) improves the situation only moderately (the color value stays more in the greenish range in these areas).

As a final example, Fig. 7 shows PS-OCT images from a scarred human skin. The scar was caused by an accident with an angle grinder which generated a deep cut into the finger skin. It has a width of ~1.5 mm. The images were taken from a 3D data set covering a volume of 8(x) × 2(y) × 1.6(z, optical distance) mm^3. Figures 7(a), 7(b), and 7(c) are single frame B-scans of reflectivity, retardation, and axis orientation, respectively; Fig. 7(d) is a DOPU image where a 3D evaluation window (window size: 3(z) × 5(x) × 5(y) pixels) was used. A Band-Aid was used to mark the rim of the scar. The Band-Aid is visible on the right hand side of the image. It is strongly depolarizing, as seen by the polarization scrambling in Figs. 7(b), 7(c), and in the DOPU image. The scar tissue shows areas of strong birefringence, especially recognizable in the retardation image as an area of increased retardation oscillations. This birefringence varies locally and is considerably stronger than that of the surrounding normal epidermis and dermis. It probably reflects the different arrangement of collagen fibers in the area of the scar and gives rise to varying patterns of retardation and axis orientation. Media 1, Media 2, and Media 3 show fly-through movies of the 3D data set, depicting reflectivity, retardation, and axis orientation data.

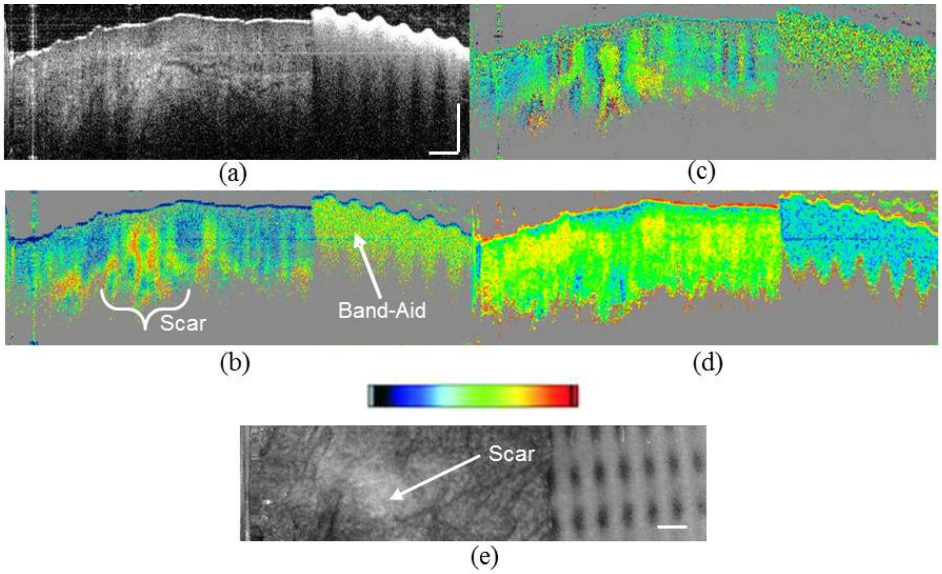

Fig. 7. PS-OCT images of human skin. Scar region; Band-Aid on right side. (a) reflectivity (log scale) (Media 1); (b) retardation (color scale: 0°–90°) (Media 2); (c) axis orientation (color scale: –90° to +90°) (Media 3); (d) DOPU (color scale: 0–1). (d) DOPU; 3D window (5(x) × 5(y) × 3(z) pixels or 40 × 40 × 19 μm^3); (e) en face projection image. Scale bar dimensions: 0.5 mm (x: geometrical distance; z: optical distance).

4. Discussion

We have presented a new high-speed swept source PS-OCT system at 1300 nm that employs a PM FDML laser and whose interferometer, sample-, reference-, and detection arm components are based entirely on PM fibers. The method is adapted from our previous spectrometer based retinal PS-OCT [50] to enable dual balanced detection. A related system has recently been reported [53] that uses a PM fiber based interferometer in combination with bulk optics polarizing beam splitters and normal single mode (SM) fibers. An advantage of using PM fibers throughout the system is that the use of polarization paddles which would otherwise be needed to optimize the light power is avoided. Another advantage lies in the use of an FDML laser with a PM cavity and a PM buffer stage. This provides a passive polarization stabilization and thereby avoids any possible rotation or change of polarization state over the sweep range.

The PS-OCT system operates at an imaging speed of 109 kA-scans/s. One of the advantages of the high imaging speed is the ability to record 3D data sets that are densely sampled in x and y directions. This is of special advantage for acquisition of DOPU images. This type of image usually has the drawback of reduced resolution because it requires averaging of Stokes vector elements within an evaluation window that spans several pixels both in horizontal (x) and vertical (z) directions. This is necessary to cover several independent speckles whose polarization state distribution is measured and averaged. Fast 3D imaging allows to reduce the extension of the evaluation window within a B-scan and instead to use a 3D window. In this way, a similar number of independent speckles can be obtained by reducing the window extension within the B-scan (x-z) and instead extending the window in y direction by taking information from adjacent B-scans into account. This improves the resolution and image quality of DOPU images considerably (cf. Fig. 5). However, in case of birefringence variations on a very narrow scale, the still limited transversal resolution can cause image artifacts (cf. Fig. 6).

With a speed of 109 kA-scans/s, the technology is not yet at its limits. In fact, the buffer stage used would also allow 4x and 8x buffering, enabling speeds beyond 400 kA-scans/s, faster FDML lasers would enable MHz scan rates. To handle these speeds for larger 3D data sets, special programming technologies to handle the data transfer between the DAQ on-board memory and the PC are required which are presently under development.

The main advantage of fiberized OCT systems is, apart from simpler alignment, the possibility of coupling to flexible probes that can access parts of the human body that are inaccessible by bulk optics systems. One of the goals of our current project will be to couple the PS-OCT engine described in this paper to endoscopic probes. Our system should be useful for both, rigid and flexible endoscopic probes. While it should be easily possible to couple rigid endoscopes to the PM fiber of the sample arm of our system, not all types of flexible endoscopes are useful. Catheter types where the sample fiber is rotated to achieve side-viewing circumferential scans [10,60] cannot be used because of the non-rotation symmetric structure of the required PM fiber. However, probes where a mirror at the fiber tip is rotated [61] should be equally usable with PM fibers and therefore useful for our system.

Because flexible probes induce variable bending of the PM fibers during handling, and because of possible temperature drifts, a one-time calibration of the phase offset (which is needed for axis orientation measurements [50]) is not stable over longer operation times. Therefore, the measured axis orientation is only relative. While this should be sufficient for most practical applications, continuous absolute calibration would also be possible by placing an additional partial reflector (e.g., a glass plate) at the probe tip whose reflection could be used for calibration monitoring. (The DOPU value should not be influenced because it doesn't require absolute phase values for each pixel; instead, DOPU just quantifies the randomness of adjacent pixel values.)

Acknowledgment

Financial support from the European Union (project FUN OCT, FP7 HEALTH, contract no. 201880) is gratefully acknowledged.